Available online at www.sciencedirect.com
SCIENCE DIRECT®
Journal of Computational Physics 192 (2003) 677–694
JOURNAL OF COMPUTATIONAL PHYSICS
www.elsevier.com/locate/jcp

Analysis of central and upwind compact schemes

T.K. Sengupta *, G. Ganeriwal, S. De

Department of Aerospace Engineering, I.I.T. Kanpur, Uttar Pradesh 208016, India

Received 15 May 2003; received in revised form 29 July 2003; accepted 29 July 2003

Abstract

Central and upwind compact schemes for spatial discretization have been analyzed with respect to accuracy in spectral space, numerical stability and dispersion relation preservation. A von Neumann matrix spectral analysis is developed here to analyze spatial discretization schemes for any explicit and implicit schemes to investigate the full domain simultaneously. This allows one to evaluate various boundary closures and their effects on the domain interior. The same method can be used for stability analysis performed for the semi-discrete initial boundary value problems (IBVP). This analysis tells one about the stability for every resolved length scale. Some well-known compact schemes that were found to be G-K-S and time stable are shown here to be unstable for selective length scales by this analysis. This is attributed to boundary closure and we suggest special boundary treatment to remove this shortcoming. To demonstrate the asymptotic stability of the resultant schemes, numerical solution of the wave equation is compared with analytical solution. Furthermore, some of these schemes are used to solve two-dimensional Navier–Stokes equation and a computational acoustic problem to check their ability to solve problems for long time. It is found that those schemes, that were found unstable for the wave equation, are unsuitable for solving incompressible Navier–Stokes equation. In contrast, the proposed compact schemes with improved boundary closure and an explicit higher-order upwind scheme produced correct results. The numerical solution for the acoustic problem is compared with the exact solution and the quality of the match shows that the used compact scheme has the requisite DRP property.

Keywords: Finite difference methods; Stability and convergence of numerical methods; Error analysis; Wave propagation

1. Introduction

With the advent of powerful computers it is now common to solve differential equations numerically in various disciplines of science and engineering. This includes the solution of partial differential equations with stringent requirements of resolving wide range of spatial and temporal scales. For example, in CFD it is now common to solve the governing Navier–Stokes equation resolving all the scales of a turbulent flow in DNS for moderate Reynolds numbers. Similarly in many wave propagation problems one solves governing

* Corresponding author. Tel.: +91512-2597561; fax: +91512-2598482.
E-mail addresses: tksen@iitk.ac.in, mpetks@nus.edu.sg (T.K. Sengupta), sde@iitk.ac.in (S. De).

0021-9991/$ - see front matter
doi:10.1016/j.jcp.2003.07.015

hyperbolic partial differential equations and such solutions are required to be accurate in the far field and for long time periods. These requirements demand that the adopted numerical method be highly accurate and dispersion error free. Lighthill [1] and Taflove [2] have discussed, respectively, the problems of computational aero-acoustics (CAA) and computational electromagnetics (CEM) for numerical solutions with respect to these issues.

Such requirements are best satisfied by spectral methods [3,4]. Spectral methods have been used mostly for problems involving simple geometries and boundary conditions, though applications to complex domains are available [26,27]. Alternatives to spectral method are the (i) higher-order explicit upwind methods as in [5,6] and (ii) methods based on Padé approximation as was originally given in [7]. The latter methods offer higher-order approximations to differential operators using compact stencils that relate various derivatives with function values at discrete nodes. All higher-order compact schemes can be expressed by the following set of linear algebraic equation

$$[A]u' = [B]u. \tag{1}$$

Each row of this represents an implicit relation between the derivatives and function values for computational nodes. For numerical convenience, it is desired that A and B be band-limited. The most often used structure of A matrix is tridiagonal. This equation can also be written down in an equivalent explicit form by

$$u' = [A]^{-1}[B]u = [C]u, \tag{2}$$

where C is not necessarily compact. The early work on compact differencing scheme can be seen in [8–10]. Such methods have been optimized to solve the time-domain Maxwell equations in [11] and for problems relating to acoustics in [12,13,28]. In [12] the important concept of dispersion relation preservation (DRP) is discussed with respect to high accuracy schemes for acoustics problems.

For problems with periodic boundary conditions, A and B are periodic symmetric matrices. However, for many practical problems periodic boundary conditions are not applicable and one-sided stencils are needed near boundaries, making A and B matrices non-symmetric. Computationally, symmetric B matrix corresponds to non-dissipative central schemes and non-symmetric B matrix arises from upwind schemes. Schemes given in [9,10,14] are typical examples of central non-dissipative method of spatial discretization. In [14] a periodic problem is solved and hence the symmetric stencil is used at all points. However, in [9] a non-periodic problem is solved that requires taking asymmetric stencils at and near-boundary points while the inner stencil is still symmetric. Such forced upwinding near boundaries can cause the overall method to become unstable. One of the aim here is to use a Fourier spectral frame-work to analyze schemes including inner and boundary closure schemes simultaneously. For upwind compact schemes, B matrix is asymmetric for all the nodes. Typical examples are as in [15,16].

Issue of whether to use a central or upwind compact scheme rests on numerical stability of such schemes everywhere in the domain. Numerical stability is usually investigated in two ways. The first is the method given in [17] that is based on normal modal analysis and referred to as G-K-S stability theory. In this theory estimates are developed for inner and boundary schemes to ensure stability. First-order partial differential equations were considered [17] as IBVPs for which the term involving the spatial derivative is multiplied by a square Hermitian matrix. For compact high-order schemes, any problem with non-periodic boundary would require an asymmetric stencil and hence the corresponding matrix is not Hermitian. For example, Carpenter et al. [18] considered two spatial discretizations that lead to the above matrix being asymmetric. The subsequent semi-discrete eigenvalue analysis (by considering a time continuous system) for the explicit and compact fourth-order spatial operators by the authors revealed a spectrum with some eigenvalues crossing over the imaginary axis into the right half plane (Figs. 3 and 4 of [18]) indicating instability. Investigated spatial discretization schemes were, however, stable in the Kreiss sense.

This brings one to the important aspect of asymptotic stability analysis. The strong point of the G-K-S analysis is that this presents a theory that includes interior points and boundaries together. But, the definition of G-K-S stability (also known as Lax stability) might be too weak [18] and hence it will not be a practical option to use those compact schemes for DNS, CAA and CEM that are only G-K-S stable. According to [18], for truly time dependent problems, sufficiently accurate solutions over long time requires excessively large number of grid points. Basically the essential dynamics of the system is then expressed over a small fraction of grid-resolved wave numbers of the very fine grid. However, the fine grid requirement negates the basic advantages of compact schemes with fewer grid points.

The time-stability analysis given in [15,18] are in the physical plane and do not provide information about the performance of schemes at different length scales. Here we adopt a different approach of investigation for spatial discretization schemes in spectral plane following the method of [19], allowing us to look at interior and boundary points simultaneously. Spatial discretization schemes for interior and boundary points may be found stable when analyzed in isolation. But, overall numerical stability may be lost when these are analyzed together. In this context a few well-known schemes are analyzed here for their accuracy and stability.

Working in the physical plane with a uniform grid of size h, the unknown is related to its bi-lateral Laplace transform by

$$u(x_l) = \int U(k) \mathrm{e}^{\mathrm{i}kx_l} \, \mathrm{d}k, \tag{3}$$

where the integral is performed over the limit $-k_m$ to k_m, defined by the Nyquist limit of $k_m = \pi/h$. Hence a first derivative is obtained analytically by $u'(x_l) = \int \mathrm{i}kU(k)\mathrm{e}^{\mathrm{i}kx_l} \, \mathrm{d}k$.

If the first derivative is evaluated numerically by discrete method, then the same can be written as

$$u'(x_l) = \int \mathrm{i}k_{\mathrm{eq}} U(k) \mathrm{e}^{\mathrm{i}kx_l} \, \mathrm{d}k. \tag{4}$$

Different numerical schemes have different estimates of k_{eq} and it is in general a complex quantity. For numerical stability of any scheme, one must look at the imaginary part of k_{eq}. The imaginary part of k_{eq} represents numerical dissipation only when it is negative. Any scheme, that produces a positive imaginary part of k_{eq} is numerically unstable because a positive imaginary part is equivalent to adding *anti-diffusion*. This method of analysis for spatial discretization is independent of the actual differential equation that has to be solved and it also indicates the length scales at which instability arises.

In the next section accuracy in spectral space is discussed considering some well-known compact schemes and some schemes that we propose here for spatial discretization. In Section 3, the numerical stability for the solution of linear wave equation is discussed for the spatial schemes used in conjunction with Euler time integration scheme. The DRP property of these space–time discretization schemes are analyzed with respect to linear wave equation in Section 4. In Section 5, numerical solution of linear wave equation is compared with exact solution for discontinuous initial data. We demonstrate the ability of two compact schemes and an explicit higher-order upwind scheme in solving the Navier–Stokes equation for the receptivity of a shear layer to a convecting vortex in the free stream. Finally, we solve an acoustics problem and compare with exact solution to show the effectiveness of the computing schemes.

2. Accuracy of compact schemes in spectral space

To evaluate k_{eq} for compact schemes for first derivative in Eq. (4), the implicit relation between the first derivatives and the function values at different nodes can be expressed by the equivalent explicit relation as given in Eq. (2). To perform spectral analysis one uses Eq. (3) in Eq. (2) – giving rise to an

implicit relation between the derivative at a given point with function values of the whole domain. One can relate the derivative at the lth-node in terms of the function value there by using a projection operator (P_{jl}) such that

$$u'_l = \left\{ \sum_{j=1}^{N} C_{lj} P_{jl} \right\} u_l, \tag{5}$$

where

$$P_{jl} = \mathrm{e}^{\mathrm{i}(j-l)kh} = R_{jl} + \mathrm{i} I_{jl}.$$

Thus, one obtains k_{eq} for any node from

$$(k_{\mathrm{eq}})_l = -\mathrm{i} \sum_{j=1}^{N} C_{lj} P_{jl} \tag{6}$$

for $l = 1$ to N. Here a value of N is chosen sufficiently large so that the results presented for k_{eq} does not depend upon this choice. Here we have used 30 points with the 1st and the 30th point as boundary points. The 2nd and the 29th points are referred to as near-boundary points in the discussion that follows. Rest of the points are treated as the interior points.

In presenting the results, we will refer to A-scheme that is given in [9]; the HT-scheme that is given in [14] and the Z-scheme given in [15]. For these schemes the real and imaginary parts of k_{eq}/k are obtained from Eq. (6) and plotted as a function of $k\Delta x$ in Figs. 1(a) and 2(a), respectively. A scheme that has a larger range over which k_{eq}/k is close to one is more accurate in spectral space and this definition of accuracy is not related to the formal accuracy defined in terms of truncation error. In these figures results for an inner and a central point are shown. The HT-scheme has the best overall resolution among these three schemes. However, all the three schemes display *anti-diffusion* for the point $j = 3$, with Z-scheme showing the least desirable property. It is evident that these schemes retain near-spectral accuracy up to large wave numbers within the Nyquist limit for the central points. The points near the boundaries show poor spectral resolution and *anti-diffusion*. For advection problems with positive group velocity the imaginary part of k_{eq} should be negative so that the feedback arising out of boundary-and near-boundary stencils is negative and numerically stabilizing. For $j = 2$ to 6 this is seen to be violated for certain ranges of high wave numbers. This will make any error present to grow due to a local instability. For receptivity problems such schemes will accumulate errors near the boundaries locally. However, if these errors convect then these errors will convect to the interior where the scheme is stable. For DNS at super-critical Reynolds numbers such sequences of instabilities and stabilities may be misinterpreted as a regeneration mechanism of fully developed turbulence.

This unstable behavior of near boundary points as faced by A-, HT- and Z-schemes are entirely due to boundary and near-boundary compact schemes and it can be removed by choosing suitable explicit stencils at boundary and near-boundary points. We propose the following boundary stencil:

$$u'_1 = \frac{(-3u_1 + 4u_2 - u_3)}{2h}. \tag{7}$$

For the near-boundary point, the following stencil is suggested:

$$u'_2 = \left[\left(\frac{2\beta}{3} - \frac{1}{3} \right) u_1 - \left(\frac{8\beta}{3} + \frac{1}{2} \right) u_2 + (4\beta + 1) u_3 - \left(\frac{8\beta}{3} + \frac{1}{6} \right) u_4 + \frac{2\beta}{3} u_5 \right] \Big/ h. \tag{8}$$

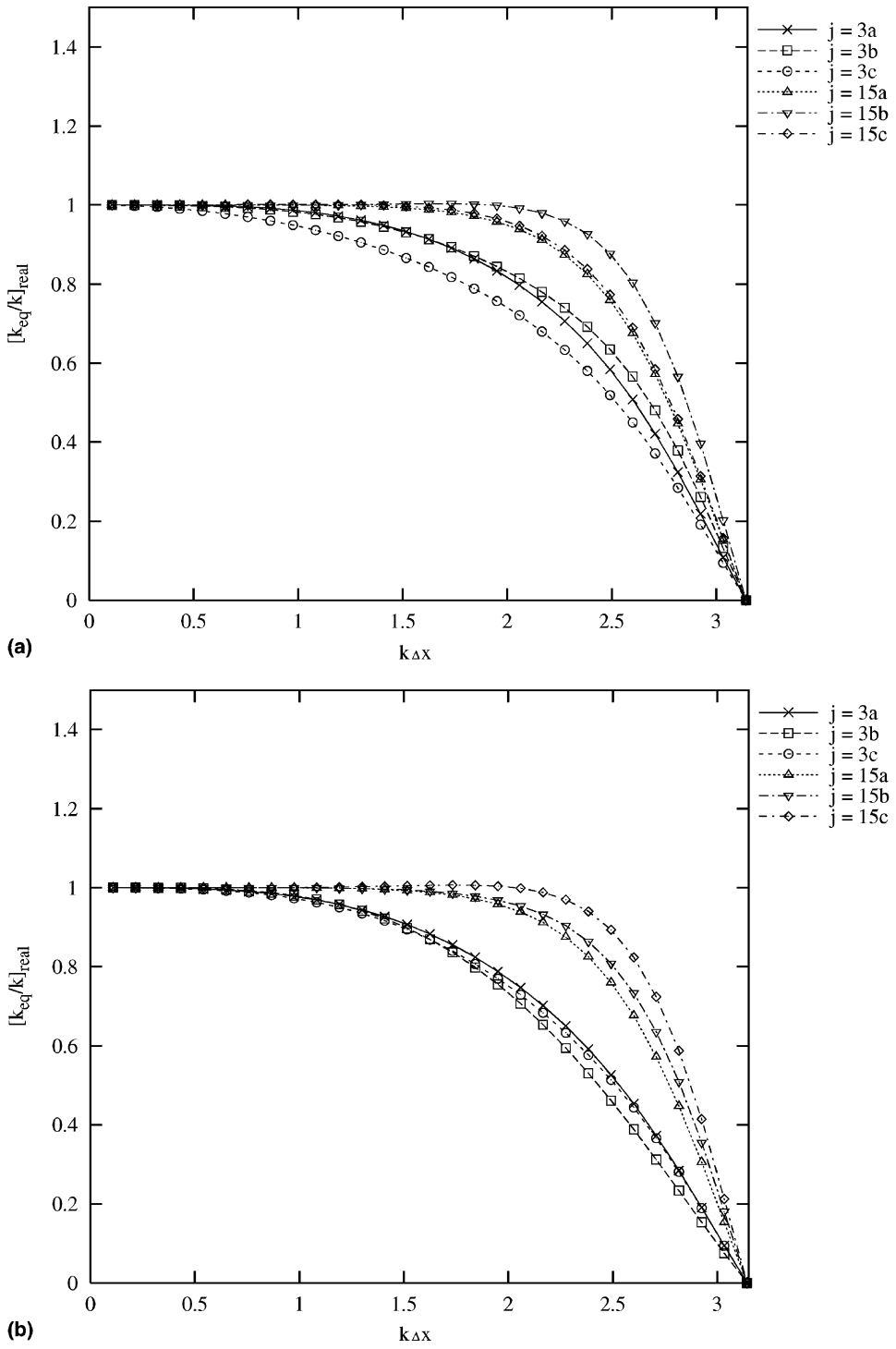

Fig. 1. (a) Real part of k_{eq}/k for the first derivative for points $j = 3$ and 15 for: (a) A-scheme, (b) HT-scheme and (c) Z-scheme. (b) Real part of k_{eq}/k for the first derivative for points $j = 3$ and 15 for: (a) OUCS-1, (b) OUCS-2 and (c) OUCS-3 schemes.

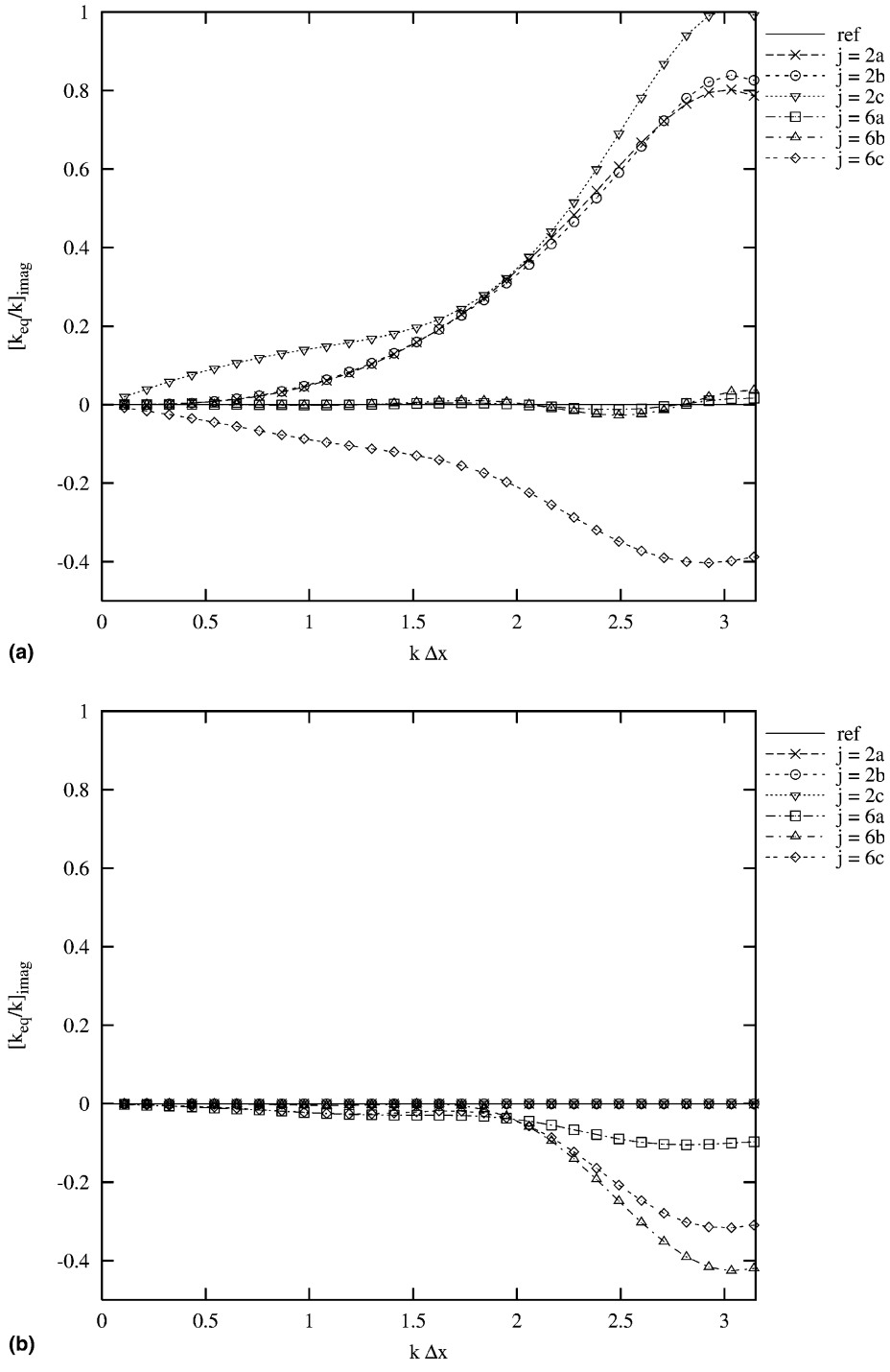

Fig. 2. (a) Imaginary part of k_{eq}/k for the first derivative at different nodes evaluated for the points $j = 2$ and 6 for: (a) A-scheme, (b) HT-scheme, (c) Z-scheme. (b) Imaginary part of k_{eq}/k for the first derivative at different nodes evaluated for the points $j = 2$ and 6 for: (a) OUCS-1, (b) OUCS-2 and (c) OUCS-3 schemes.

These boundary and near-boundary stencils along with the following interior stencils are to be used in our proposed schemes. For the first such scheme – referred to as the first optimized upwind compact scheme or OUCS1 – the interior stencil is given by

$$b_{l-1}u'_{l-1} + b_l u'_l + b_{l+1}u'_{l+1} = \frac{1}{h}\sum_{k=-2}^{2} a_{l+k}u_{l+k} - \frac{\alpha}{6!}h^4\left(\frac{\partial^6 u}{\partial x^6}\right) \tag{9}$$

with $a_{l\pm2} = \pm\frac{5}{3} + \frac{5}{6}\alpha$; $a_{l\pm1} = \pm\frac{140}{3} + \frac{20\alpha}{3}$; $a_l = -15\alpha$; $b_{l\pm1} = 20 \pm \alpha$ and $b_l = 60$. This is an upwind scheme for $\alpha < 0$ and is based on a sixth-order central scheme (with $\alpha = 0$). In Z-scheme $\alpha = -0.24$ is used. The Z-scheme in turn is an upwind version of the A-scheme proposed in [9]. The value of β in Eq. (8) used here is -0.09 for $j = 2$ and 0.12 for $j = 29$.

The second proposed scheme is also a variant of the Z-scheme with the following inner stencil:

$$b_1 u'_{l-1} + b_2 u'_l + b_3 u'_{l+1} = \frac{1}{h}\sum_{k=-2}^{2} a_k u_{l+k}, \tag{10}$$

where $b_1 = \frac{b_2}{3} - \frac{\alpha_1}{12}$; $b_3 = \frac{b_2}{3} + \frac{\alpha_1}{12}$; $a_{\pm2} = \mp\frac{b_2}{36} + \frac{\alpha_1}{72}$; $a_{\pm1} = \mp\frac{7b_2}{9} + \frac{\alpha_1}{9}$ and $a_0 = -\frac{\alpha_1}{4}$. This scheme is referred to as OUCS2. Unlike the Z-scheme, here the coefficient of $\partial^6 u/\partial x^6$ term is treated as the free parameter α_1. The optimal behavior with respect to phase and dispersion error is seen for $\alpha_1 = -40$ and $b_2 = 36$. The value of β in Eq. (8) is chosen as 0.02 for $j = 2$ and 0.09 for $j = 29$.

The third optimal upwind scheme (referred to as OUCS3) is a variation of the HT-scheme. Here the inner stencil is given by

$$p_{l-1}u'_{l-1} + u'_l + p_{l+1}u'_{l+1} = \frac{1}{h}\sum_{k=-2}^{2} q_k u_{l+k}, \tag{11}$$

where $p_{l\pm1} = D \pm \frac{\eta}{60}$; $q_{\pm2} = \pm\frac{F}{4} + \frac{\eta}{300}$; $q_{\pm1} = \pm\frac{E}{2} + \frac{\eta}{30}$ and $q_0 = -\frac{11\eta}{150}$ and with $D = 0.3793894912$; $F = 1.57557379$; $E = 0.183205192$ and $\eta = -2$. Here, in Eq. (8) $\beta = -0.025$ for $j = 2$ and $\beta = 0.09$ for $j = 29$ is used for optimal performance.

The six compact schemes discussed above are for problems where information propagation is uni-directional. For many practical convection dominated problems information propagates in all direction and then explicit schemes are robust and useful. A third-order upwind scheme used in [5,6,20] referred here as K-scheme has the following interior stencil:

$$u'_l = \frac{(-u_{l+2} + 8u_{l+1} - 8u_{l-1} + u_{l-2})}{12h} + \frac{(u_{l+2} - 4u_{l+1} + 6u_l - 4u_{l-1} + u_{l-2})}{4h}. \tag{12}$$

For near-boundary points in [6,20] first-order upwinding is used for stability. All the compact schemes discussed above have excellent accuracy in spectral space-better than explicit high-order schemes. The formal accuracy of compact schemes revealed by Taylor series expansion is not relevant. Because, OUCS3 and HT-schemes are only second-order accurate but they provide the highest accuracy in spectral space among these six schemes. In designing the OUC schemes the following procedure is adopted. Once the C matrix in Eq. (2) has been constructed each row represents a stencil for a point corresponding to that row number. To avoid instability for the near-boundary points the corresponding rows are replaced by an explicit second-order central difference stencil. Use of Eq. (8) is mandatory in constructing the C-matrix for stable behavior of other points in the domain.

3. The numerical stability and amplification properties

To evaluate any numerical scheme it is natural to calibrate it with respect to a model equation that mimics the physical processes and preferably possesses exact solution. The linear wave equation serves these requirements. For DNS, physical convection is most important and a method is preferred that solves wave equation most effectively. With this in mind we use different compact schemes to discretized spatial derivative while using standard temporal schemes for the wave equation

$$\frac{\partial u}{\partial t} + c\frac{\partial u}{\partial x} = 0, \tag{13}$$

where c is the phase speed of the propagating wave.

If we relate the unknown in Eq. (13) with its bi-lateral Laplace transform by

$$u(x,t) = \int U(k,t)\mathrm{e}^{\mathrm{i}k(x-ct)}\,\mathrm{d}k, \tag{14}$$

then we can define the amplification factor of any numerical scheme by $G = U(k,t+\Delta t)/U(k,t)$. This amplification factor depends upon the spatial and temporal discretization used in Eq. (13). For Euler time integration scheme this is obtained, by using Eq. (6) in Eq. (13), as

$$G(k) = 1 - c\Delta t\sum_j C_{lj}\mathrm{e}^{\mathrm{i}k(x_j - x_l)}. \tag{15}$$

The real part of the amplification factor for all the seven schemes are shown for CFL number (N_c) equal to 0.001 in Fig. 3 for the Euler time integration scheme. It is already shown that some spatial discretization

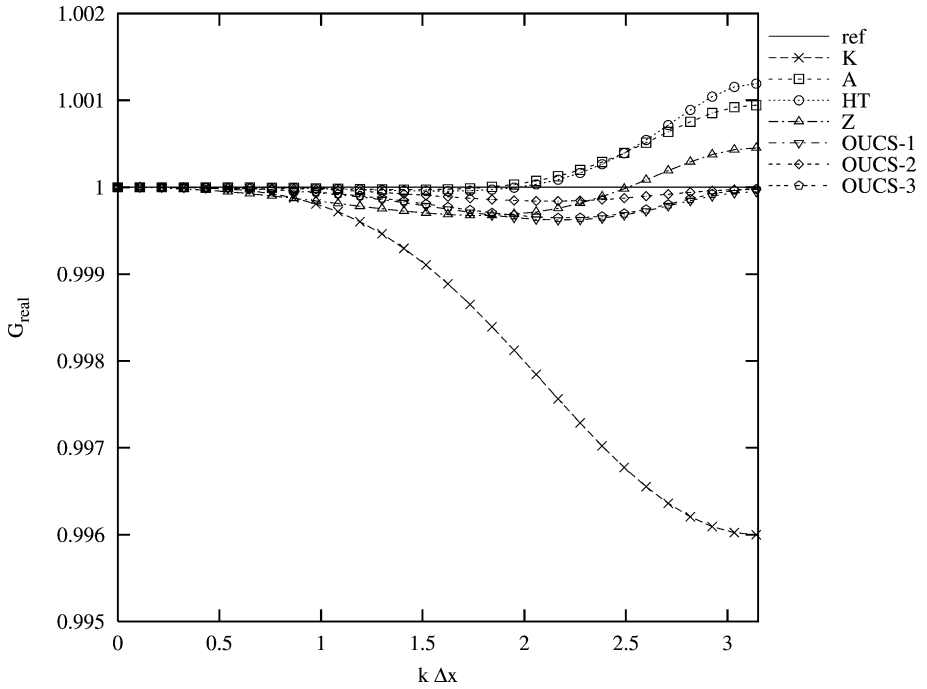

Fig. 3. Real part of amplification factor (G) at the point $j = 3$ for various spatial schemes, in solving linear wave equation using Euler time integration scheme. All OUC schemes are stably clustered below $G = 1$.

schemes have instability built-in due to the addition of *anti-diffusion* at points near the boundaries. When such schemes are used in conjunction with time discretization schemes the resultant schemes can become stable or unstable depending upon the nature of the temporal discretization. In this context, the Euler time discretization, for very small time steps, is neutral i.e. it transmits the spatial discretization properties without any modifications. Among the different spatial schemes in Fig. 3, A-, HT- and Z-schemes show instability for many points at high wave numbers. The K- and OUC schemes are stable across all wave numbers. The instability can be avoided by taking large number of points such that the essential dynamics of the system is represented within the stable wave number range itself [18]. However, this defeats the main purpose of higher-order schemes that allows solving problems with fewer points due to their higher accuracy in spectral space. A stable and robust scheme should damp out undesirable high wave number error components that are due to aliasing error. At the same time, it should not suppress physical oscillations. Thus, a useful numerical scheme should be near-neutral at small and moderate wave numbers while it should have adequate amount of dissipation present at high wave numbers.

Multi-stage Runge–Kutta time integration schemes have been used often for its excellent stability properties. If a four stage time integration strategy is used for these compact schemes, then the corresponding amplification factor is given by

$$G_4 = (1 - 2ay + 2bz) - 2\mathrm{i}(by + az), \tag{16}$$

where $y = 1 - [2a - 2a^2 + 2b^2 + a^3 + 3ab^2]/3$ and $z = [4ab - 2b - 3a^2b + b^3]/3$ and $a + \mathrm{i}b = N_c h/2 \sum_j^N C_{lj} \mathrm{e}^{\mathrm{i}kh(j-l)}$. These are shown in Fig. 4 for CFL number equal to $N_c = 0.001$. The features are same as in Fig. 3. However, the high wave number instability for A-, HT- and Z-schemes is more severe for this time integration scheme.

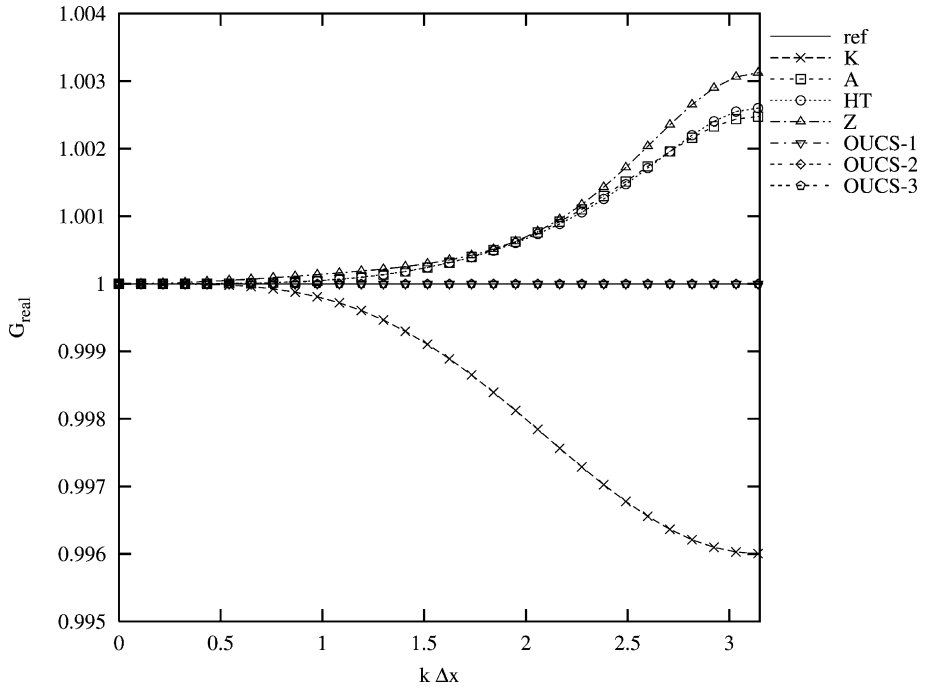

Fig. 4. Real part of amplification factor (G) at the near boundary point ($j = 2$) for various spatial schemes, in solving linear wave equation using Runge–Kutta four stage time integration scheme for CFL No. $= 10^{-3}$. All OUC schemes are stably clustered at $G = 1$.

4. Dispersion relation preservation property of numerical schemes

For many wave propagation problems the group velocity (V_g) is a more meaningful physical quantity than the phase speed – as energy propagates with this velocity. In this context linear wave equation is non-dispersive i.e. the group velocity and phase speed are identical. Thus if we use Eq. (13) as the model equation, then a numerical scheme for space–time dependent problem can be characterized by comparing the numerical group velocity with the phase speed. Spectral method shows equality of numerical and physical group velocity identically for Eq. (13). This is not the case for other discrete computational methods. Methods have been identified in [12] as dispersion relation preserving (DRP) if numerical and physical dispersion relation matches. Here, instead of looking at the dispersion relation the group velocity estimate is used as a quantifier for DRP property. Such an analysis was performed in [21] for flux vector splitting finite volume schemes that use higher-order reconstruction of fluxes at the cell interface.

DRP property is specific for governing equations and for Eq. (13) this is given by

$$\omega = kc. \tag{17}$$

The dispersion relation is the governing differential equation in the spectral plane indicating space–time scale interrelationship for truly unsteady problems. Thus it is imperative that high accuracy schemes satisfy this. The numerical group velocity of a scheme is estimated by evaluating $\mathrm{d}k_{\mathrm{eq}}/\mathrm{d}k(= p + \mathrm{i}q)$ by using Eqs. (5) and (6) and $\mathrm{d}\omega_{\mathrm{eq}}/\mathrm{d}\omega(= r + \mathrm{i}s)$ for the used time discretization scheme. The numerical group velocity is then given by

$$(V_g)_{\mathrm{Num}} = \frac{pr + qs}{r^2 + s^2}. \tag{18}$$

Two time integration methods are listed below with their value of $\mathrm{d}\omega_{\mathrm{eq}}/\mathrm{d}\omega$:

- Euler scheme: Here $r + \mathrm{i}s = \cos(\omega\Delta t) - \mathrm{i}\sin(\omega\Delta t)$.
- Adams–Bashforth scheme [22]: Here $r = [a_3c_3 + b_3d_3]/[a_3^2 + b_3^2]$ and $s = [a_3d_3 - b_3c_3]/[a_3^2 + b_3^2]$, where $a_3 = 9+\cos(2\omega\Delta t) - 6\cos(\omega\Delta t)$; $b_3 = \sin(2\omega\Delta t) - 6\sin(\omega\Delta t)$; $c_3 = 8\cos(\omega\Delta t) - 4$ and $d_3 = -4\sin(\omega\Delta t)$.

For the Runge–Kutta schemes the numerical group velocities are evaluated directly using Eq. (13) and calculating V_g. If we define

$$\begin{aligned} a_4 + \mathrm{i}b_4 &= h\sum_j C_{lj}\mathrm{e}^{\mathrm{i}k(x_j - x_l)}, \\ a_5 + \mathrm{i}b_5 &= \sum_j C_{lj}(x_j - x_l)\mathrm{e}^{\mathrm{i}k(x_j - x_l)}, \end{aligned} \tag{19}$$

then for the four stage Runge–Kutta scheme the numerical group velocity is obtained as $(V_g)_{\mathrm{Num}} = c[a_5 + 2N_c(b_4b_5 - a_4a_5)/3 + a_5N_c^2(3a_4^2 - b_4^2 - N_ca_4^3 + N_ca_4b_4^2)/6 + b_4N_c^2(-6a_4b_5 - 2b_4a_5 - 3N_ca_4^2b_5 - N_cb_5b_4^2 + 2N_ca_4a_5b_4)/6]/\cos(\omega\Delta t)$.

The numerical group velocity is compared with phase speed in the $(k\Delta x - \omega\Delta t)$-plane in Fig. 5 for the A- and OUCS3 schemes for spatial discretization and the above three time discretization schemes. The useful region is darkened in this plane where the numerical group velocity is within $\pm 5\%$ of the exact value. The region close to the origin is of interest. For both the spatial discretization schemes, Euler and RK_4 time discretization schemes have identical ranges of wave number and circular frequency available for DRP. However, the Adams–Bashforth time integration scheme has poor DRP property for both the spatial discretization schemes. It is noted that the DRP analysis is performed only for the interior stencils.

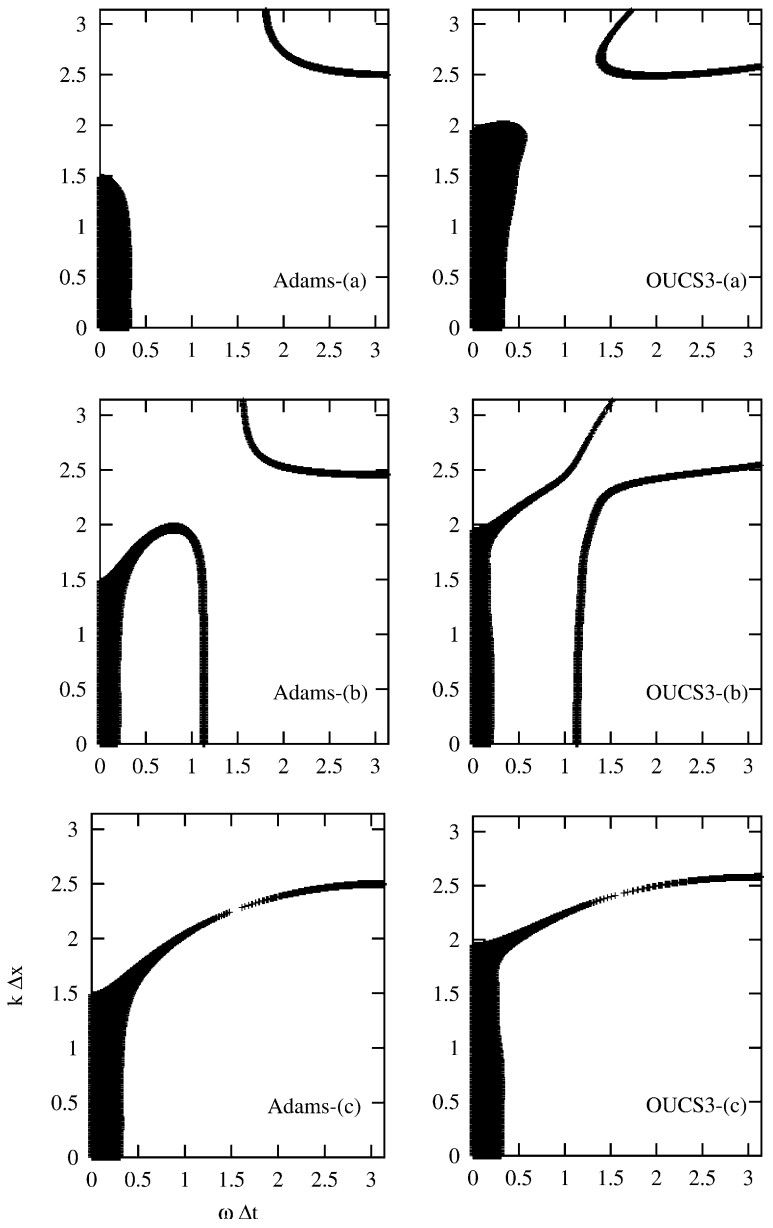

Fig. 5. Region of ($k\Delta x$–$\omega\Delta t$) plane where numerical group velocity is within 5Euler (b) Adams–Bashforth (c) Runge–Kutta four stage time integration schemes. CFL number taken for Runge–Kutta method is 0.001.

5. Solution of linear wave equation

The analyses of the previous sections have shown that the Euler time integration scheme has near-neutral amplification factor and good DRP property for low computational efforts. In solving linear wave equation Euler time integration is considered here to highlight certain features of spatial schemes by comparing the computed results with exact solution.

Here a domain of $0 \leqslant x \leqslant 1$ is considered with 200 uniformly distributed points. The phase speed is taken as $c = 0.05$ such that the signal given by the initial condition (as shown in the top panel of Fig. 6) leaves the computational domain at $t = 20$. The initial condition has piecewise discontinuity at both the ends and is identically zero outside the domain. This discontinuous initial condition excites a large range of wave numbers. The number of grid points chosen is large to provide a Nyquist limit on wave number equal to 200π so that the aliasing error is not important. The analytical solution is identically zero in the computational domain for $t \geqslant 20$. Thus a long time integration would reveal asymptotic stability of numerical methods.

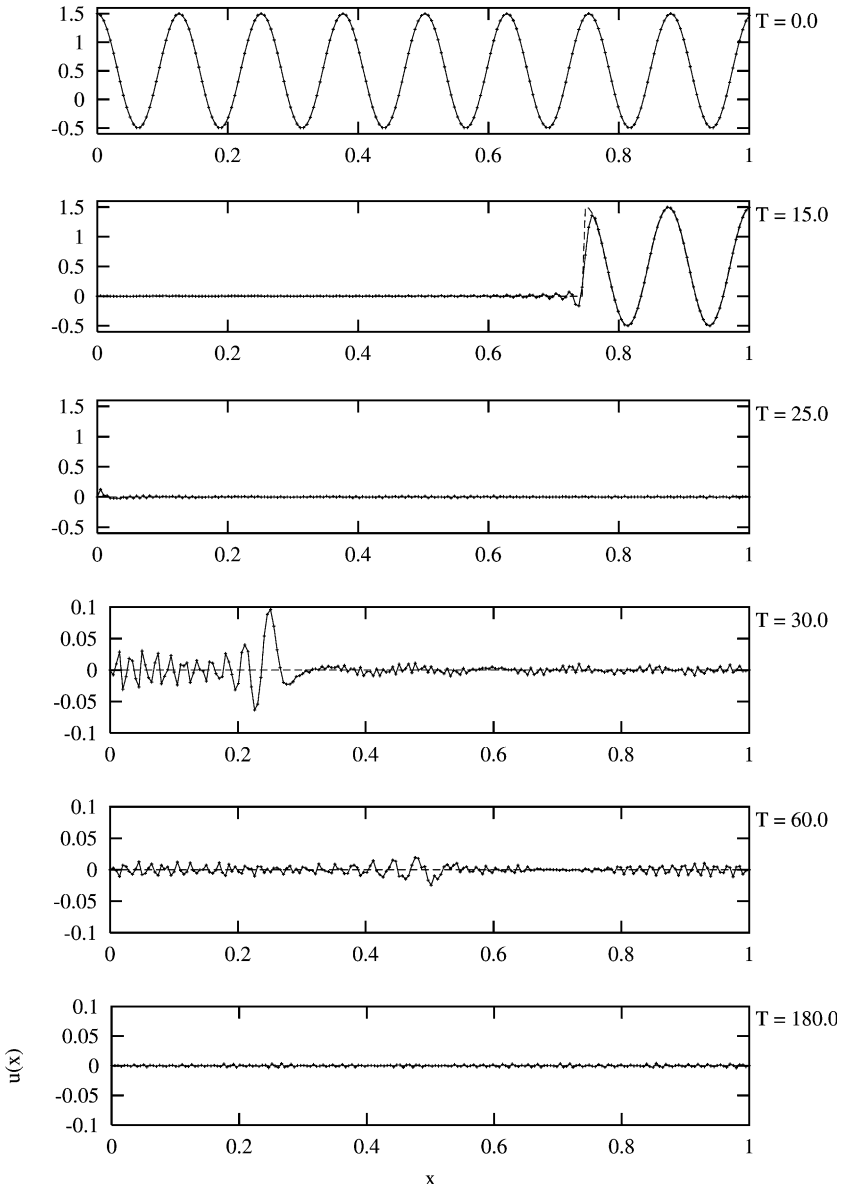

Fig. 6. Plots of $u(x)$ vs x for the linear wave equation. Computed results, using Adams compact spatial scheme and Euler time integration, are compared with the analytical solution for phase speed $c = 0.05$; no. of spatial nodes = 200 and time step = 10^{-4}. Last three panels are magnified.

The numerical and exact solution of Eq. (13) are compared in Fig. 6 for the A-scheme. The discontinuity of the initial condition at the left boundary propagates inside the computing domain with time. One notes the associated Gibbs phenomenon to the left of the discontinuity. Subsequently when the discontinuity has moved inside, the present numerical dissipation will attenuate the solution locally. The fact that this scheme is unstable for $j = 2$ is visible from the solution shown at $t = 25$. This is also visible at $t = 30$, where the y-scale is enhanced. Beyond $t = 20$ the solution is zero in the computational domain. However, round-off and other numerical errors constitute a wide-band noise over the whole domain that is amplified near the left boundary (where Fig. 2(a) indicated numerical instability) and noted beyond $t = 20$. With time this error moves to the right where lesser or no instability is seen. The effect of such instability is seen as far as the first quarter of the domain. This error attenuates more and more as it moves to the right due to the low pass filter nature of the scheme and also due to numerical dissipation introduced.

In Fig. 7 the computed wave solution by HT-scheme is compared with the exact solution. As before one notices the Gibbs' phenomenon to the left of the propagating discontinuity. The HT-scheme has higher

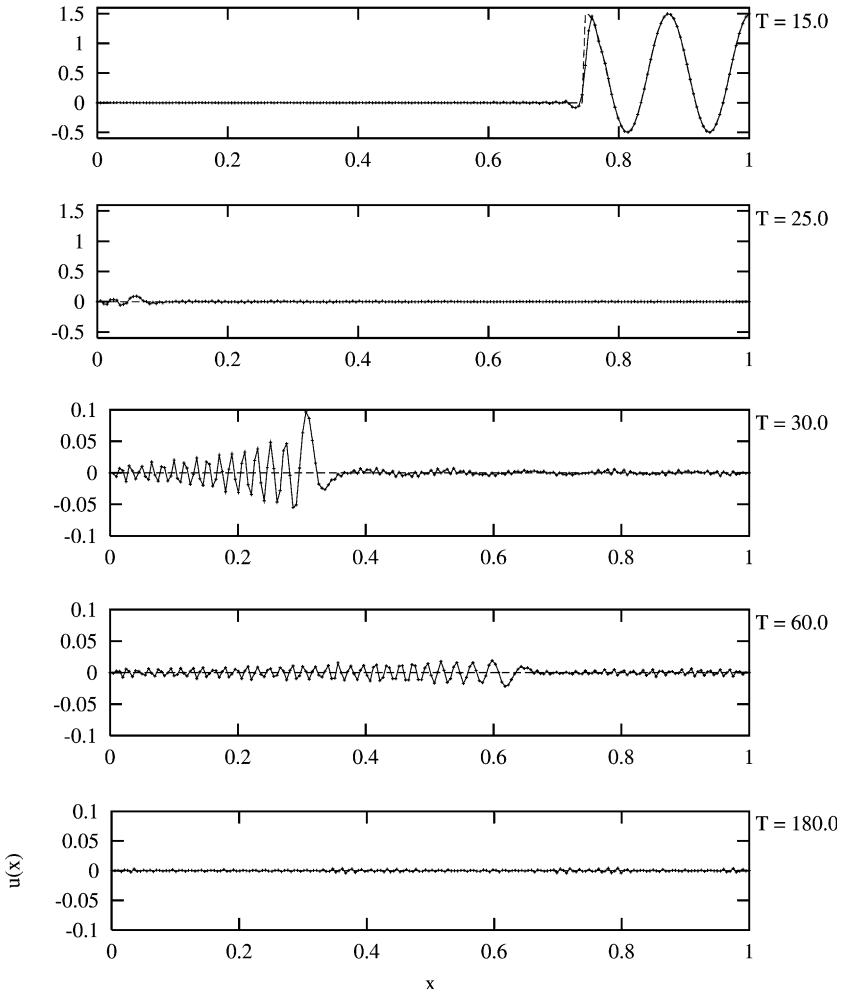

Fig. 7. Plots of $u(x)$ vs x for the linear wave equation. Computed results, using Haras–Ta'asan compact scheme and Euler time integration, are compared with the analytical solution for the same parameters as in Fig. 6.

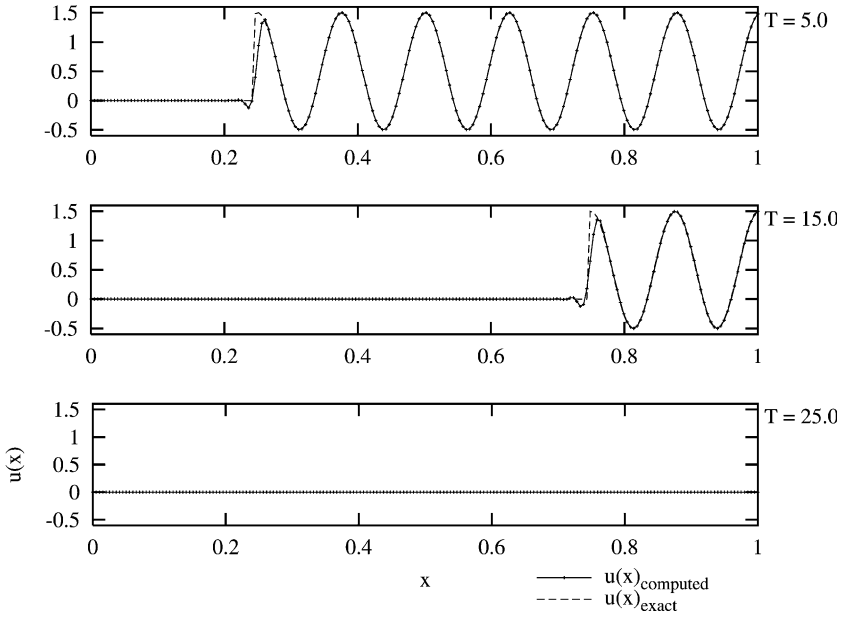

Fig. 8. Plots of $u(x)$ vs x for linear wave equation. Computed results, using OUCS-2 compact spatial scheme and Euler time integration, are compared with exact solution for the same parameters as in Fig. 6.

spectral resolution as compared to the A-scheme. But HT-scheme also has larger instability near the left boundary as compared to the A-scheme. This is the reason for larger error that propagates farther to the right. The low-pass nature of the associated filter of this scheme causes the error to eventually decay for large time.

Fig. 8 shows the corresponding solution for OUCS2 that has the least amount of numerical dissipation among the OUC schemes. Thus one notices very good agreement between computed and exact solution. Also the Gibbs phenomenon is minimal here with very few oscillations upstream and smaller amplitudes as compared to A- and HT-schemes. The solution displays no error beyond $t = 25$. Both of these features are due to the added numerical dissipation of this scheme at inner and boundary stencils.

6. Some examples

6.1. Receptivity of shear layer

Vortex-induced eruptions inside a shear layer, as excited by a convecting vortex far outside the shear layer is an important problem with many applications. This has been investigated earlier theoretically [23,24] and experimentally [25]. This is a typical receptivity problem and can be used to check the efficiency of some of the compact schemes to solve Navier–Stokes equation. Here the Navier–Stokes equation in stream function-vorticity (ψ–ω) formulation has been solved using the K-scheme [5,6,20], the A-scheme [9] and the OUCS3 scheme for the vorticity transport equation.

Here the problem is solved in a box located above a flat plate. In the computational domain, uniform grid is used in the streamwise direction using 800 points for the K-scheme and 400 points for the compact schemes. In the wall normal direction a non-uniform grid that stretches in an arithmetic progression is used for all the cases. For the K-scheme 175 points have been used in this direction with wall resolution of

$0.00175\delta^*$, where δ^* is the displacement thickness of the shear layer at the inflow of the domain that is $84\delta^*$ from the leading edge of the plate. The Reynolds number based on this length scale is 250 and the flow is sub-critical with respect to Tollmien–Schlichting waves up to $x/\delta^* = 369$. For the A-scheme and OUCS3 we have used only 100 points in the wall normal direction.

For the boundary and initial conditions, the effect of single convecting vortex above the shear layer at a constant height of $32\delta^*$ is calculated analytically considering an image vortex. This provides Dirichlet boundary conditions at the top and inflow boundary of the domain. At the inflow the oncoming shear layer is given by the Blasius profile. At the outflow (located at $384\delta^*$ from the leading edge) a fully developed condition is used for the normal velocity. This fixes the vorticity at outflow boundary by the kinematic definition of vorticity. The initial condition is obtained over the whole computational domain by using the boundary layer solution everywhere and adding the inviscid perturbation to it that is created by the convecting vortex and its image. The image vortex ensures that there is no normal velocity at the solid wall at all times. Note that the convecting vortex is located at $x = 50\delta^*$ at $t = 0$. This vortex convects to the right at a speed of $c = 0.20U_\infty$.

The stream function equation is solved by the conjugate gradient method. For the solution of vorticity transport equation we have treated the diffusion terms by central differencing. The convection terms have been discretized by the third-order upwinding [5,6,20] for the K-scheme. These terms are separately evaluated by solving the implicit equations for the compact schemes. For a general problem the convection velocity switches direction that is not known a priori. The A-scheme being a central scheme for the interior

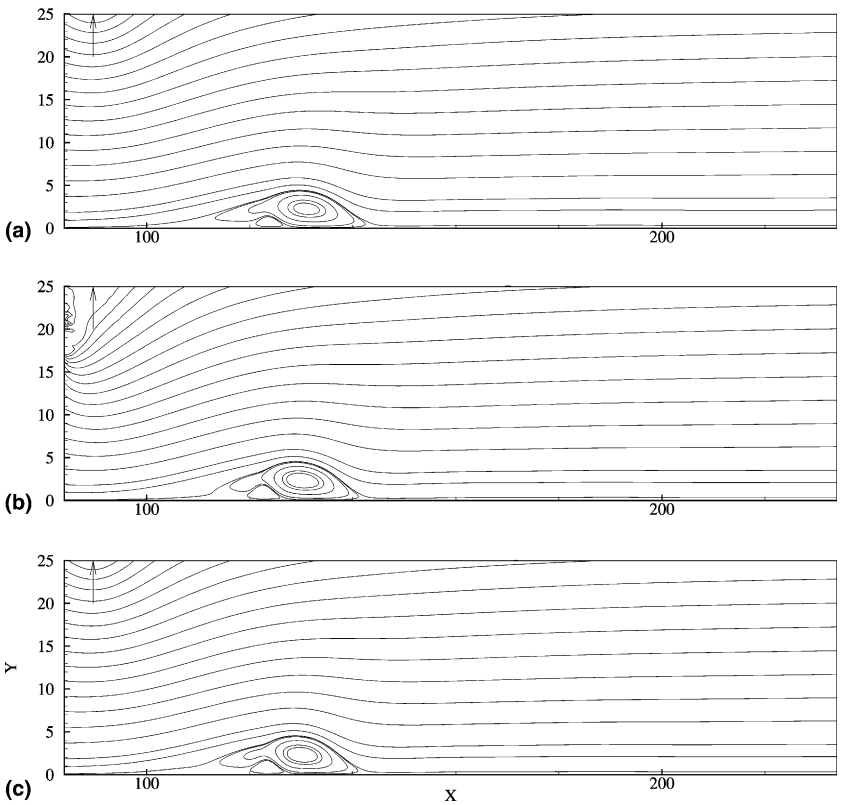

Fig. 9. Streamline contours at indicated times for: (a) Kuwahara, (b) Adams and (c) OUCS3 schemes as obtained by solving the Navier–Stokes equation in ψ–ω formulation. The arrow on the top left corner indicates the location of the convecting vortex.

with fixed boundary stencils such an information is not needed. But, for the OUCS3 one has to calculate derivatives at each time step by calculating the sign of local velocity vector.

The results are shown in Fig. 9 for $t = 198$ just prior to when the A-scheme blew up due to numerical instability – as evident from the stream function contour plots. The difficulty starts near the top left corner of the domain, where the unstable effects of the near-boundary points were shown in Fig. 2(a). The imposed excitation is large at this time when the convecting vortex is above the computational domain. The K- and OUCS3 schemes continue beyond this time without any instability.

6.2. Linear acoustics

To demonstrate the performance of the proposed schemes for a two-dimensional hyperbolic problem a simple linear aero-acoustics problem is solved next that admits an exact solution. This is obtained by solving the full Euler equation. We consider the simultaneous propagation of acoustic, entropic and

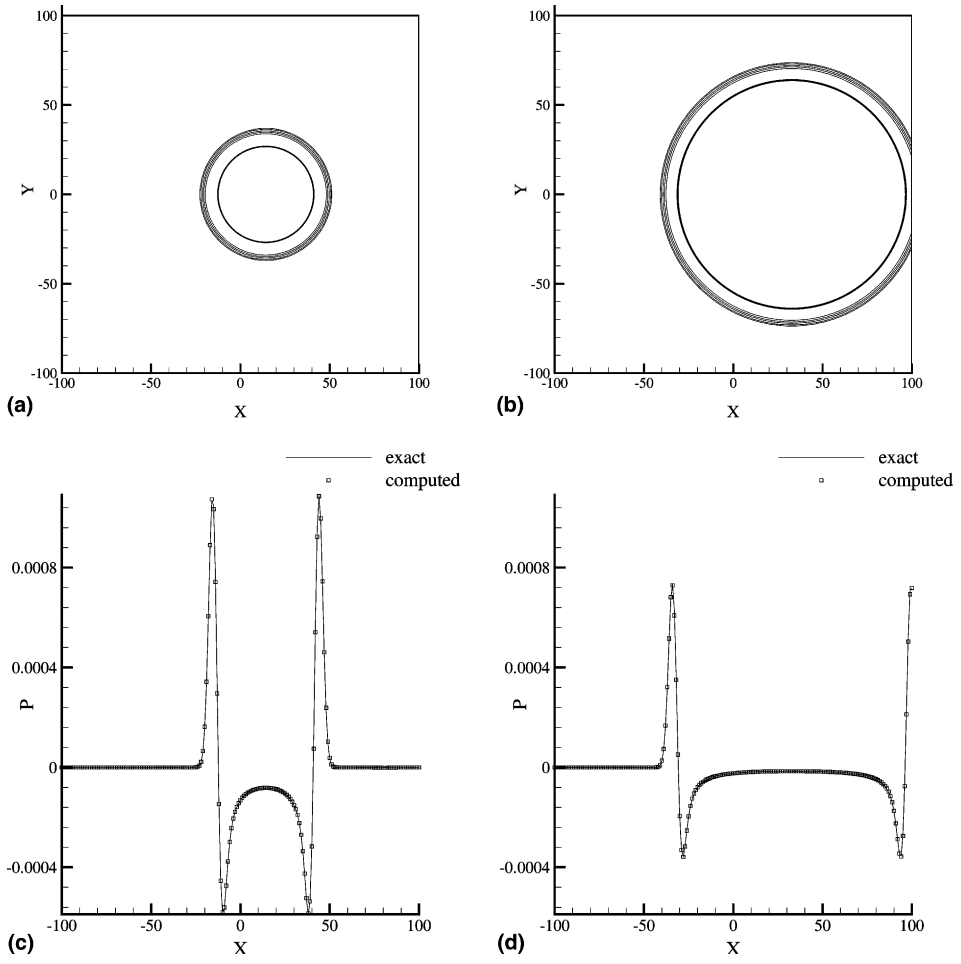

Fig. 10. Solution of Euler equatin for the acoustic problem of [12]. In (a) and (b) pressuredisturbance contours at 500 and 1150 time steps, respectively, are shown for the peak amplitude and 20%, 10%, 5%, 2% and 1% levels of it. In (c) and (d) the computed solution is compared with the exact solution at these times at the centerline.

vortical wave pulses. This is the problem that was considered in [12] to discuss about the DRP property of numerical schemes and the boundary conditions. We have used the OUCS2 scheme given by Eq. (10) along with $\alpha_1 = 0$. To avoid spurious reflections from the boundaries optimized nine point stencils have been used that is given by

$$u' = \frac{1}{h}\sum_{l=1}^{9} a_l u_l. \tag{20}$$

All the a_l's are obtained from consistency requirements by Taylor series expansion with $a_1 = -2.62538939007719$. Similar stencils were developed for two more layers of points on all boundary segments. The mean flow ($M_\infty = 0.5$) is superposed initially with pressure, vorticity and entropy pulses of amplitudes 0.001, 0.001 and 0.0004, respectively. The respective half widths of the Gaussian pulses are 3, 3 and 5. We have used the same uniform grid as used in [12] with the spacing as the length scale. The velocity scale is provided by the speed of sound of the undisturbed flow. For further details the reader is referred to [12]. The time integration of Euler equation was performed by the DRP-scheme proposed in [12].

In Fig. 10 some representative contour and line plots are shown for the disturbance pressure at indicated times using the DRP-time integration scheme with $\Delta t = 0.0569$. The computed results match identically with the computed solution in [12] for the contours shown in Figs. 10(a) and (b). In Figs. 10(c) and (d) the computed disturbance pressure along the center-line is compared with the exact solution of the linearized Euler equation. The excellent match between the two indicates the ability of our proposed scheme to tackle two-dimensional hyperbolic problems.

7. Conclusions

Central and upwind compact schemes have been analyzed by a matrix- spectral analysis developed here. It is shown that some of these schemes are unstable due to boundary stencils near one of the boundaries. To cure this problem – arising from the boundary treatment – three new optimal upwind-biased schemes have been proposed (OUCS1, OUCS2 and OUCS3 defined in Eqs. (10)–(12)).

The combined space–time discretization methods for linear wave equation show the amplification factor to be unstable near the boundary as well. Also we show that the group velocity, an indicator of DRP property (in the sense that is described in [12,21]), can be used to describe the space–time discretization effectiveness for truly unsteady problems. It is found that the proposed upwind-biased schemes in conjunction with Euler time integration scheme have the desirable property of near-neutral stability and DRP property. This is tested by solving linear wave equation with discontinuous initial condition. It is also seen that some of the schemes are not stable asymptotically. This is also shown by solving Navier–Stokes equation for a well-defined receptivity and an acoustic wave problem.

References

[1] M.J. Lighthill, Computational Aeroacoustics, Springer, New York, 1993.
[2] A. Taflove, Computational Electrodynamics: The Finite-DifferenceTIme-Domain Method, Artech House, Boston, 1995.
[3] D. Gottlieb, S.A. Orszag, Numerical Analysis of Spectral Methods, SIAM, Philadelphia, 1977.
[4] C. Canuto, M.Y. Hussaini, A. Quarteroni, T.A. Zang, Spectral Methods in Fluid Dynamics, Springer, New York, 1987.
[5] T. Kawamura, H. Takami, K. Kuwahara, Fluid Dyn. Res. 1 (1985) 145.
[6] M.T. Nair, T.K. Sengupta, J. Fluids Struct. 11 (1997) 555.
[7] Z. Kopal, Numerical Analysis, second ed., Wiley, New York, 1961.
[8] R.S. Hirsch, J. Comput. Phys. 19 (1975) 90.
[9] Y. Adam, J. Comput. Phys. 24 (1977) 19.

[10] S.K. Lele, J. Comput. Phys. 103 (1992) 16.
[11] D. Gaitonde, J.S. Shang, J. Comput. Phys. 138 (1997) 617.
[12] C.K.W. Tam, J.C. Webb, J. Comput. Phys. 107 (1993) 262.
[13] K.-Y. Fung, R.S.O. Man, S. Davis, AIAA J. 34 (1996) 2029.
[14] Z. Haras, S. Ta'asan, J. Comput. Phys. 114 (1994) 265.
[15] X. Zhong, J. Comput. Phys. 144 (1998) 662.
[16] N.A. Adams, K. Shariff, J. Comput. Phys. 127 (1) (1996) 27.
[17] B. Gustafsson, H.O. Kreiss, A. Sundstrom, Math. Comp. 26 (119) (1972) 649.
[18] M.H. Carpenter, D. Gottlieb, S. Abarbanel, J. Comput. Phys. 108 (1993) 272.
[19] R. Vichnevetsky, J.B. Bowles, Fourier Analysis of Numerical Approximations of Hyperbolic Equations, SIAM, Philadelphia, 1982.
[20] T.K. Sengupta, R. Sengupta, Comput. Mech. 14 (4) (1994) 298.
[21] T.K. Sengupta, S. Sridar, S. Sarkar, S.De I, J. Numer. Meth. Fluids 37 (2) (2001) 149.
[22] G.J. Haltiner, R.T. Williams, Numerical Prediction and Dynamic Meteorology, Wiley, New York, 1980.
[23] V.J. Peridier, F.T. Smith, J.D.A. Walker, J. Fluid Mech. 232 (1991) 99.
[24] V.J. Peridier, F.T. Smith, J.D.A. Walker, J. Fluid Mech. 232 (1991) 133.
[25] T.K. Sengupta, T.T. Lim, M. Chattopadhyay, An experimental and theoretical investigation of a by-pass transition mechanism, I.I.T. Kanpur Report No. IITK/Aero/AD/2001/02, 2001.
[26] S.A. Orszag, J. Comput. Phys. 37 (1980) 70.
[27] A. Ditkowski, K.H. Dridi, J.H. Hesthaven, J. Comput. Phys. 170 (2001) 39.
[28] R. Hixon, E. Turkel, J. Comput. Phys. 158 (2000) 51.